ADVANCED FUNCTIONAL MATERIALS
www.afm-journal.de

A Biomimetic Epidermal Sensing Sucker via Stress Excitation for Personalized Cardiovascular Monitoring

Yiqian Wang, Yang Zou, Jiangtao Xue, Zhenmin Fan, Puchuan Tan, Minghao Liu, Peng Cheng, Han Ouyang, Yifan Fan, Aiping Liu, Yulin Deng, and Zhou Li**

Personalized cardiovascular monitoring plays an critical role in early detection and management of cardiovascular diseases. However, current noninvasive monitoring methods face challenges of unstable sensor-skin interfaces, physiological and anatomical differences, and difficulty in balancing accuracy and comfort. Here, inspired by octopus suckers' mechanics, we present a biomimetic epidermal sensing sucker (BESS) that integrates conformal physiological sensing with in situ pressure modulation. The stable attachment to the arterial site is achieved through negative-pressure adsorption, while the amplitude of the pulse signal is enhanced for optimal detection via adaptive pressure modulation, effectively addressing interindividual variability. Drawing on Traditional Chinese Medicine pulse palpation, BESS applies incremental vertical pressure to induce stress excitation in local arterial vessels, capturing pulse oscillation waves and quantifying traditional pulse diagnostic information. Leveraging the enriched pulse features acquired by BESS, a cuffless blood pressure (BP) estimation system is developed by integrating classical oscillometry with pulse wave feature analysis through machine learning, achieving high accuracy (1.36 ± 3.81 mmHg for systolic BP and 1.15 ± 2.94 mmHg for diastolic BP) without occluding arterial blood flow. The interdisciplinary integration of biomimetics and intelligent sensing technology provides a promising pathway for personalized cardiovascular monitoring with balanced accuracy, comfort, and interpretability.

1. Introduction

Cardiovascular diseases (CVD) continue to be the leading cause of death worldwide. Personalized cardiovascular health monitoring is crucial for the early warning and long-term management of CVD.[1–3] Pulse physiological signals provide real-time insights into hemodynamic parameters such as heart rate, cardiac rhythm, and peripheral vascular resistance, serving as vital indicators for the assessment of cardiac pumping function, circulatory status, and vascular elasticity. While wearable technologies such as photoplethysmography (PPG)[4,5] and pressure sensors[6–8] have achieved noninvasive pulse monitoring, they are often limited by the stability of the interface between the skin and the sensor, variations in arterial anatomy across individuals, and the lack of diversity in signal characteristics under normal conditions, making it challenging to meet clinical demands. Pulse depth and intensity may vary significantly between individuals due to differences in gender, age, body fat, etc.[9,10]

Y. Wang
Center on Nanoenergy Research
School of Physical Science and Technology
Guangxi University
Nanning 530004, China

Y. Wang, P. Tan, P. Cheng
Beijing Institute of Nanoenergy and Nanosystems
Chinese Academy of Sciences
Beijing 101400, China

Y. Zou, Z. Li
Beijing Tsinghua Changgung Hospital
School of Clinical Medicine
School of Biomedical Engineering
Tsinghua Medicine
Tsinghua University
Beijing 100084, China
E-mail: zya05204@btch.edu.cn; li_zhou@tsinghua.edu.cn

J. Xue, Y. Deng
School of Medical Technology
Beijing Institute of Technology
Beijing 100081, China

The ORCID identification number(s) for the author(s) of this article can be found under https://doi.org/10.1002/adfm.202514598

DOI: 10.1002/adfm.202514598

Z. Fan
School of Mechanical Engineering
Jiangsu University of Technology
Changzhou, Jiangsu 213001, China

P. Tan, P. Cheng, H. Ouyang
School of Nanoscience and Technology
University of Chinese Academy of Sciences
Beijing 100049, China

M. Liu
Department of Biomedical Engineering
Chinese University of Hong Kong
Hong Kong 999077, China

Y. Fan
Department of Cardiology
Heart Center and Beijing Key Laboratory of Hypertension
Beijing Chaoyang Hospital
Capital Medical University
Beijing 100020, China

A. Liu
Department of Electronic Engineering and Information Science
University of Science and Technology of China
Hefei 230026, China

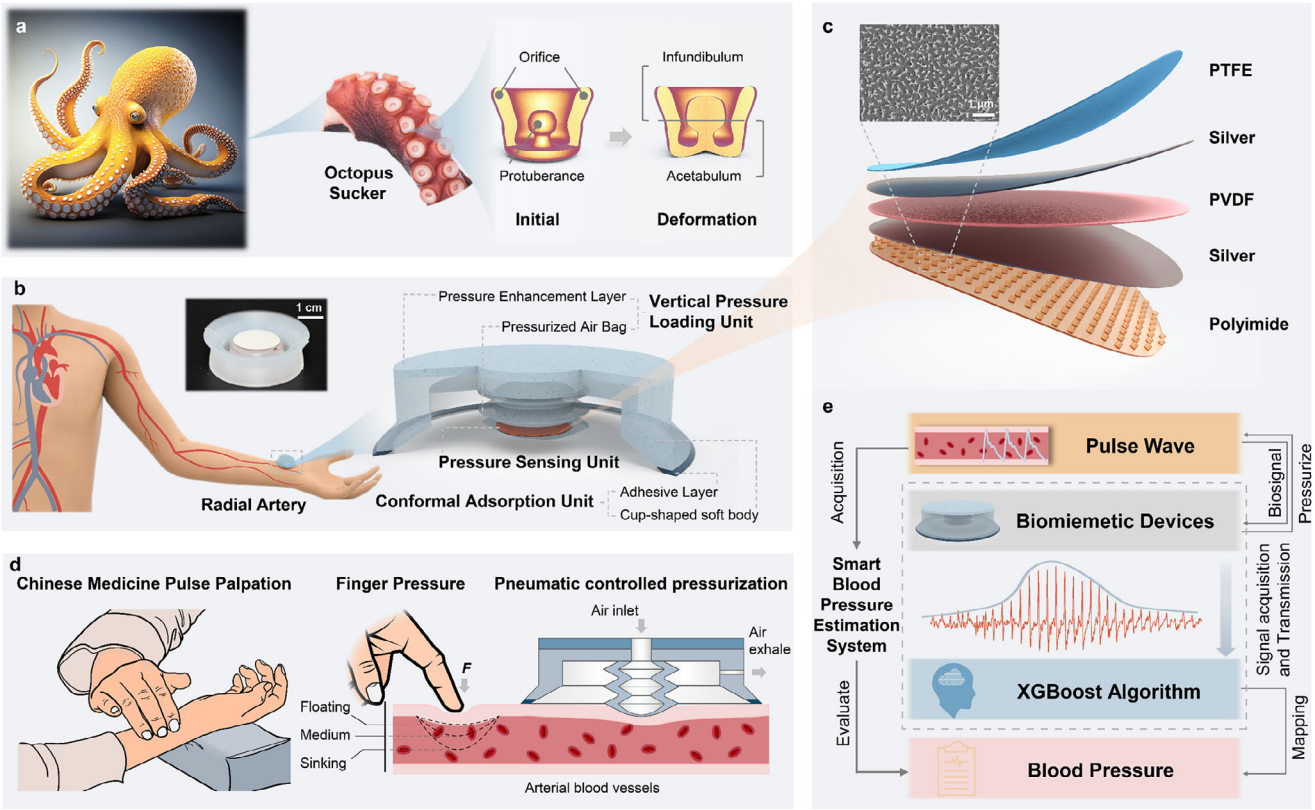

Figure 1. Design of the biomimetic adaptive pulse pressure sensor (BESS) and smart blood pressure (BP) estimation system. a) The biological inspiration for the BESS and the internal structure of the octopus sucker. b) Schematic and object demonstration of the structure of BESS. c) Structural demonstration of the pressure sensing unit and scanning electron microscope image of the polyimide surface after inductively coupled plasma (ICP) etching. d) BESS draws on the manner of pressure loading in TCM: floating, medium, sinking. The pressure applied to the skin surface of the test site is controlled by adjusting the size of the air pressure inside the BESS. e) Workflow diagram of the BESS and smart BP estimation system.

Therefore, to achieve effective detection of pulse signals across individuals, the manner of securing the sensor to the body surface, the tightness of conformal contact with skin, and the external pressure used to assist detection are crucial. Pulse diagnosis is a basic technique in Traditional Chinese Medicine (TCM) that can be used to determine an individual's health status by adjusting the pressure applied during pulse palpation to perceive subtle differences in pulse signals.[11,12] Although this method is convenient and efficient, it relies on the experience and subjective judgment of the TCM practitioner.[13,14] Furthermore, the lack of standardized paradigms for pulse palpation analysis impedes the transformation of TCM pulse diagnosis experiences into evidence-based medicine.[13]

Blood pressure (BP) serves as another vital indicator in cardiovascular monitoring, facilitating the prompt identification of risk factors such as hypertension, which can help prevent serious complications.[15–19] The human pulse is intrinsically linked to BP, and the analysis of pulse waveforms allows for the indirect evaluation of BP fluctuations.[20–22] Currently, most existing noninvasive BP detection methods are closely associated with pulse signals. As the gold standard for clinical noninvasive BP measurement, auscultation has high accuracy but relies on the operation of professional medical staff.[23,24] Oscillometry is widely used in various commercial BP detection equipment because of its convenience and automation.[25,26] However, due to the relatively single algorithm and characteristic parameters, it needs to be calibrated regularly.[27] Both methods rely on inflated cuffs to apply continuously varying external pressure on the arterial site to detect corresponding changes in the pulse wave. This process usually requires blocking the arterial blood flow, resulting in mechanical discomfort. On the other hand, some BP measurement methods enable continuous BP monitoring by correlating the pulse transit time or pulse wave features to BP, but still face challenges in terms of interpretability and accuracy in practical applications. Overall, the first category of methods focuses on studying overall pulse changes when dynamic pressure is applied, while the second category captures the detailed characterization of individual pulse waves at a constant state.[6,28] Combining the advantages of these two methods may be a potential solution to break through the accuracy, applicability, and convenience of existing BP detection, which lies in the ability to apply controlled pressure loading to the arterial site while accurately sensing changes in the pulse.

The octopus sucker has a unique infundibulum and protuberance morphology that allows for conformal adsorption, pressurization, and free detachment on various surfaces through fine muscle control, inspiring a series of innovative research including soft robotic grippers,[29,30] moisture-resistant adhesive patches,[31–35] and adhesive actuators.[36–38] In this study, inspired by the structural mechanics of octopus suckers and the

principles of TCM pulse palpation, we present the development of a biomimetic epidermal sensing sucker (BESS). The device seamlessly integrates conformal physiological sensing with in situ pressure modulation, facilitating adaptive cardiovascular monitoring across individuals. By emulating the negative-pressure adsorption and active pressurization mechanisms of octopus suckers, BESS achieves stable attachment and conformal sensing on various arterial sites through controllable in situ pressure loading. Notably, the adaptive pressure modulation capability significantly enhances pulse signal amplitude approximately threefold, addressing inter-individual variability in pulse detection to optimize measurement consistency. Drawing on TCM pulse palpation, BESS captures arterial oscillation waves by applying incremental vertical pressure to the epidermis, thereby inducing stress excitation in local vascular structures and blood flow dynamics. Further analysis of pulse signal response features during continuous pressurization enables the quantitative characterization of traditional pulse diagnostic information. Leveraging these advancements, we have also developed a novel cuffless BP estimation system that integrates classical oscillometry with pulse wave features analysis. The system effectively captures pulse oscillation waves without occluding arterial blood flow by employing an in situ localized stress excitation strategy. A robust BP correlation model has been established using machine learning, achieving high accuracy (1.36 ± 3.81 mmHg for systolic BP and 1.15 ± 2.94 mmHg for diastolic BP) while ensuring interpretability. By bridging the gap between pulse dynamics and BP estimation, BESS provides a comprehensive solution for personalized cardiovascular health monitoring.

2. Results

2.1. Biomimetic Design and Structure of BESS

BESS is inspired by the natural structure and function of octopus suckers. Unlike previously reported octopus-inspired bio-patches that typically mimic either the structural morphology or single adhesion functions, BESS achieves multifunctional biomimicry by structurally replicating the concave geometry of octopus suckers while functionally integrating negative pressure adhesion, pressure modulation, and sensing capabilities (Table S1, Supporting Information). As illustrated in **Figure 1a**, the core of the octopus sucker lies in a cup-shaped structure composed of infundibulum and acetabulum. When the soft, elastic-edged orifice comes into contact with and adheres to the object's surface, a seal cavity is formed. After that, the acetabulum and the internal protuberance deform through muscle contraction to expel the liquid and air in the cavity, reducing the cavity pressure and effectively enhancing the adsorption force. Relying on the fine control of complex muscle tissues, the octopus can contract or relax its muscles as needed to regulate the adhesion strength and internal pressure to adapt to different shapes, sizes and materials of various objects.[38] For instance, when encountering larger or rougher objects, the octopus can slightly increase the adsorption force of the sucker to ensure that the object can be firmly grasped. When encountering smaller or smoother objects, the octopus can disperse the adsorption force of the sucker and avoid excessive compression or damage to the surface of the object.

Informed by these biological principles, we designed a fully flexible BESS with self-adaptive bioinspired conformal perception, as shown in Figure 1b. By mimicking the negative pressure adsorption and active pressurization mechanism of octopus suckers, BESS achieves stable attachment and conformal sensing across diverse anatomical sites, including the temporal, brachial, and radial arteries. This approach enables effective adaptation to individual variations commonly encountered in pulse detection, significantly enhancing the pulse signal amplitude for optimal pulse measurement through adaptive pressure modulation. The BESS primarily consists of three components: the conformal adsorption unit, the vertical pressure loading unit, and the pressure sensing unit. Among them, the conformal adsorption unit is composed of a cup-shaped soft body and an adhesive layer, designed for conformal adherence and fixation on the surface of human skin. The vertical pressure loading unit is composed of a bellows-shaped pressurized airbag and a vertical pressure enhancement layer for applying controlled pressure locally on the human body. The pressure sensing unit is composed of a silver-plated polyvinylidene difluoride (PVDF) as the core sensing layer, a micro-structured polyimide (PI) substrate as the stress enhancement layer and a polytetrafluoroethylene (PTFE) film as the encapsulation layer, which is stacked to realize the effective detection of the subtle mechanical physiological signals from the human body (Figure 1c). The PVDF sensor is encapsulated by micro-structured PI and PTFE layers, both providing strong moisture and oil barriers. The sensing unit is further embedded at the distal protrusion of the vertical loading module and sealed with silicone elastomer. This multi-layer protection isolates PVDF from sweat and oil exposure, maintaining long-term signal stability and eliminating dielectric loss risks.[39,40]

2.2. Working Principle of BESS

In TCM pulse diagnosis, the pressure exerted by the TCM practitioner's fingers is critically important, as the pulse information obtained under varying pressure conditions may differ significantly. For example, the techniques known as "floating", "medium", and "sinking" represent three typical manners of pulse palpation, corresponding to light, moderate, and heavy finger pressure, respectively. Drawing on TCM pulse palpation, the BESS employs a stress excitation strategy that induces localized mechanical excitation through adaptive pressure loading to enhance the pulse signal, as shown in Figure 1d. Specifically, the BESS is initially positioned over the artery to be assessed, where the adhesive layer of the conformal adsorption unit forms a preliminary seal on the skin surface. Subsequently, a vacuum pump extracts the air from the seal cavity via a side airway, decreasing the internal pressure and thereby securing the device firmly to the skin. The vacuum pump controls the negative pressure to be maintained at −40 to −50 kPa to ensure that the pressure sensing unit fits closely on the skin, effectively preventing slippage and improving the stability of signal acquisition. Next, the vertical pressure loading unit inflates the airbag via an independent airway at the top of the BESS, applying positive pressure to the area of attachment. The pressure applied to the skin surface can be controlled by adjusting the air pressure of the airbag,

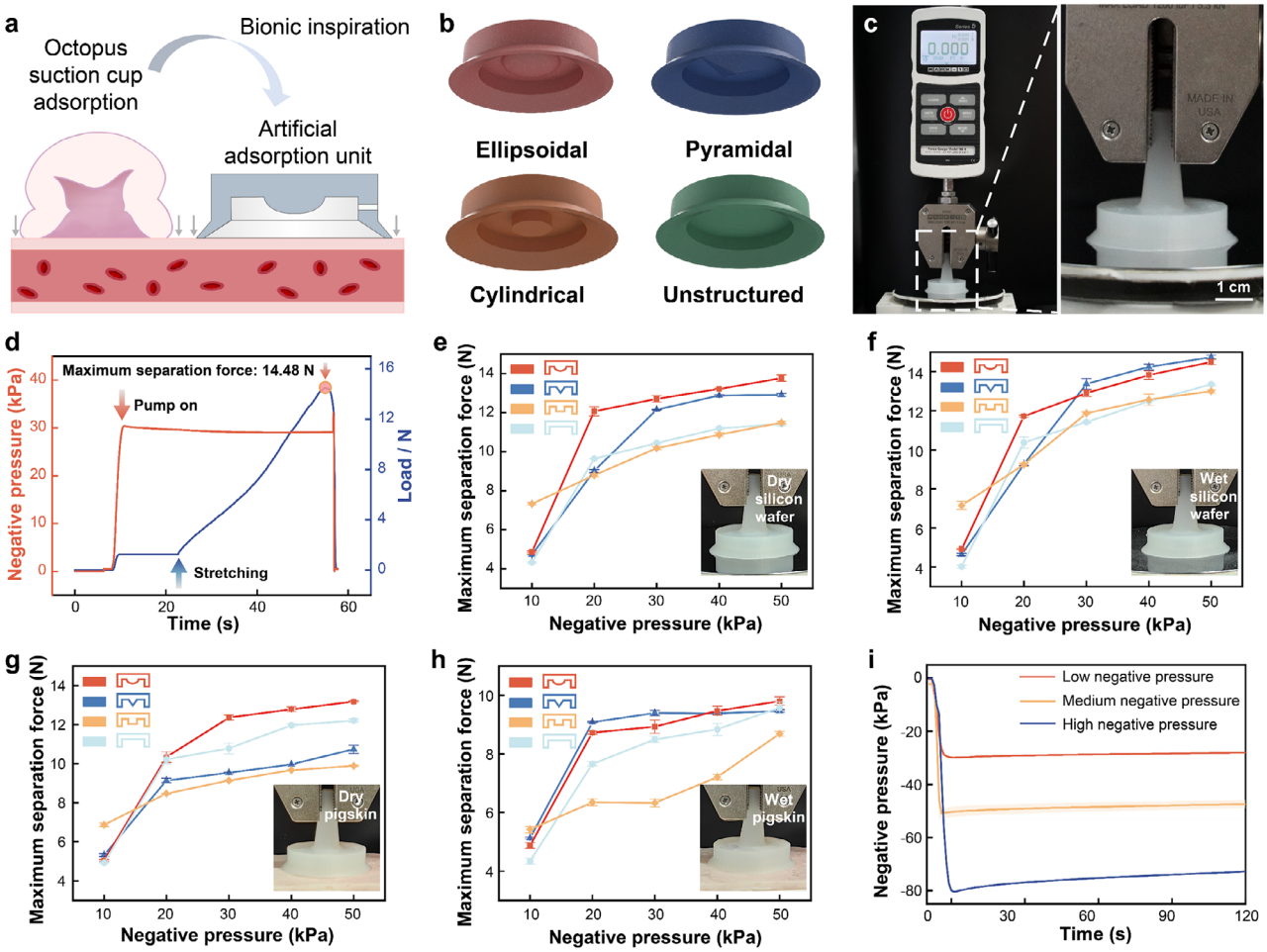

Figure 2. Characterization of the adsorption properties of the conformal adsorption unit. a) Inspiration and biomimetic design of the conformal adsorption unit. b) Schematic representation of a conformal adsorption unit with four different internal structures (ellipsoidal, pyramidal, cylindrical, and unstructured). c) Adsorption capacity test scenario of a conformal adsorption unit with the upper end fixed to the fixture and the lower part adsorbed to the test surface. d) Changes in negative pressure inside the conformal adsorption unit during the adsorption capacity test and changes in pulling force during the uniform upward pulling of the digital force gauge. e–h) Maximum separation force tests of four different structures of suction cups on the surfaces of dry silicon wafers, wet silicon wafers, dry pigskin, and wet pigskin. i) Variation of negative pressure inside the conformal adsorption unit during 120 s. e–i: Data are presented as mean ± S.E.M. (n = 3 independent experiments). The error bars represent the precision of the mean estimate.

thereby achieving precise loading of local pressure (The air circuit structure is shown in Figure S2, Supporting Information). The cup-shaped soft body of the BESS deforms through a combination of vertical compression and radial contraction during vacuum loading. The main body, constructed from a silicone elastomer with a Young's modulus of 0.59 MPa, allows progressive and reversible volume reduction as air is evacuated. To suppress excessive collapse and maintain cavity geometry under high negative pressure, a mechanical enhancement layer composed of higher-modulus PDMS (2.05 MPa Young's modulus, 148.9 MPa compressive modulus) is integrated at the top of the cavity. This reinforced region increases vertical stiffness and stabilizes deformation behavior, preventing structural buckling while preserving suction efficiency. The Young's modulus of the adhesive layer was measured at 63 kPa. It deforms synchronously with the cup-shaped soft body and adapts to the skin's morphological variations. Beyond its mechanical compliance, the adhesive layer also contributes to robust sealing under diverse skin conditions. In the presence of perspiration or body hair, it enhances adhesion through liquid-assisted interfacial filling and capillary interactions, effectively suppressing air leakage and ensuring stable negative-pressure retention. Through this localized stress excitation strategy, BESS applies increasing vertical pressure to the epidermis, stimulating mechanical responses from underlying blood vessels and blood flow to generate pulse oscillation waveforms. Utilizing the stress-enhanced piezoelectric effect, the pressure sensing unit integrated into the front end of the bellows-shaped airbag can convert subtle mechanical pulse signals directly into electrical signals with high sensitivity and rapid response. Finally, with the support of the signal acquisition and transmission circuit (The circuit design schematic is shown in Figures S3 and S4, Supporting Information), pulse signals can be effectively captured, amplified, filtered, and transmitted to the computer and other terminals in real-time. This process facilitates standardized pulse analysis by capturing the dynamic response features of pulse signals during continuous

pressurization, enabling the quantitative characterization of traditional pulse diagnosis information.

When BESS is used to apply continuously increasing pressure to the arterial site, the amplitude of the acquired pulse signal gradually increases, and then decreases after reaching the peak, which is consistent with the feature of the pulse oscillation waveforms obtained from the classical oscillometry of BP measurement (Figure 1e). To achieve a high-precision cuffless BP estimation, BESS integrates classical oscillometry with pulse wave features analysis, establishing a robust correlation with BP through machine learning models. Specifically, the Gaussian envelope is extracted from the acquired pulse oscillation waveforms to capture overall features, while individual pulse wave related features are also extracted. These features are then collectively input into a BP estimation model based on the XGBoost algorithm for training, and a smart, cuffless BP evaluation system based on BESS is constructed. In the process of BP estimation, the pulse oscillation waveform is first acquired by BESS, then the BP is accurately evaluated by the XGBoost algorithm model, and finally the results are transmitted to the user interface.

2.3. Characterization of the Conformal Adsorption Unit

In order to achieve the conformal and firm attachment of BESS on the human body surface, inspired by the remarkable adsorption capacity of the octopus sucker, we designed an artificial adsorption unit that mimics the octopus sucker (**Figure 2a**). The internal protuberance of the octopus sucker plays a crucial role in enhancing its adsorption capacity.[41] Here, while maintaining the same volume of the inner cavity, we prepared unstructured, as well as three kinds of protuberance structure (ellipsoidal, pyramidal, and cylindrical) conformal adsorption units, to verify the effect of different internal structures on adsorption performance (Figure 2b). To facilitate the test of the adsorption capacity, a structure for clamping is added to the top of the conformal adsorption unit. During the test, the adsorption unit is fixed on the clamp of the digital force gauge, and the height is adjusted to make it in contact with the test surface (Figure 2c). Then, the inner cavity pressure of the conformal adsorption unit is pumped to the specified negative pressure (−10, −20, −30, −40, and −50 kPa) through the pneumatic control module. After that, the digital force gauge is activated, and the conformal adsorption unit is slowly pulled upward at a speed of 30 mm/min until it is detached from the surface, and the maximum tension before detachment is recorded as the maximum separation force to determine the adsorption capacity, as shown in Figure 2d and Figure S5 (Supporting Information).

The maximum separation forces between the wafer and pigskin surfaces were further explored for different conformal adsorption units under dry conditions (relative humidity of ≈50%) and wet conditions (an average of 33.97% of the silicon area was covered by water droplets; Figure S6, Supporting Information) for the surfaces of dry silicon wafer, wet silicon wafer, dry pig skin, and wet pig skin, as shown in Figure 2e–h, respectively. The results showed that the ellipsoidal structure has a good adsorption effect on various test surfaces. When the inner cavity pressure is −50 kPa, the maximum separation force of the conformal adsorption unit with the ellipsoidal protuberance on the surface of dry silicon wafer, wet silicon wafer, dry pig skin and wet pig skin can reach 14.49, 13.76, 13.19, and 9.81 N, respectively. The mechanical differences in suction performance among the four cavity geometries may be attributed to their distinct deformation behaviors under negative pressure. The ellipsoidal structure showed gradual cavity collapse and uniform strain distribution, supporting stable sealing under deformation. The pyramidal structure concentrated strain near the apex, enabling strong local contact but reduced global adaptability. The cylindrical structure exhibited limited resistance to deformation, leading to early collapse and reduced suction. The unstructured cavity lacked internal modulation and exhibited irregular deformation, resulting in poor sealing and low adhesion. The magnitude of adsorption force is also affected by the type of substrate and humidity state. Under dry conditions, suction forces were slightly higher on smooth, rigid silicon surfaces compared to pigskin. This is likely due to better initial contact and reduced interfacial air gaps. Under moist conditions, suction forces decreased significantly on pigskin, likely due to surface fluid retention and slippage, whereas forces increased on silicon, where a thin moisture film may have improved contact conformity and vacuum sealing. The moisture state of the substrate directly affects the frictional interaction, which in turn affects the sealing performance. In dry conditions, high interfacial friction suppressed lateral displacement, making vertical deformation the dominant factor. Ellipsoidal cavities exhibited less vertical collapse than pyramidal ones, leading to stronger suction. In moist conditions, friction was reduced, allowing more lateral expansion. The pyramidal structure better resisted this lateral deformation due to its localized apex and rigid edges, resulting in higher suction under wet conditions compared to other geometries. These results demonstrate that suction performance arises from the coupled effects of cavity geometry, substrate type, and moisture state.

While sweat typically compromises the adhesion of conventional suction cups by introducing interfacial fluid pathways and promoting leakage, this challenge is addressed in BESS by integrating a compliant adhesive layer around the cup rim. The adhesive layer not only enhances conformal contact under dry conditions but also utilizes moisture to assist interfacial sealing. Adhesion tests performed under various skin conditions (including dry, sweaty, and hairy skin) demonstrated that the introduction of this adhesive layer significantly improves suction stability. On dry skin, the measured separation force was ≈4.86 N. Under sweaty conditions, it increased to ≈8.47 N. In the presence of hair, adhesion was further elevated, reaching ≈5.64 N on dry hairy skin and up to 9.22 N on sweaty hairy skin (Figure S7, Supporting Information). These enhancements may be attributed to several synergistic mechanisms. First, the moisture-induced capillary interactions at the skin-adhesive interface help fill micro-gaps, improving airtight contact. Second, the soft adhesive conforms dynamically to complex skin microtopography, increasing the effective contact area. Finally, the presence of hair may act as compliant microstructures that stabilize the local interface, further suppressing vacuum leakage by forming hair-bridged sealing networks. These effects collectively contribute to enhanced adhesion under realistic conditions involving perspiration and body hair. The adhesive layer exhibited a Young's modulus of 63 kPa, supporting both surface conformability and mechanical integrity

for sealing (Figure S8, Supporting Information). Optical imaging further demonstrated its ability to maintain intimate contact with irregular forearm skin, even under tensile deformation (Figure S9, Supporting Information). Long-term mechanical durability was confirmed through repeated attachment-detachment cycles under preloaded sealing, during which the separation force remained stable ≈7.15 N over 1000 cycles, with no observed delamination or performance degradation (Figure S10, Supporting Information).

To check the air tightness of the conformal adsorption unit under different negative pressures, the pressure of the inner cavity was pumped to low (−30 kPa), medium (−50 kPa), and high negative pressures (−80 kPa) through the pneumatic control module, respectively, and then the attenuation of the negative pressure of the inner cavity was recorded. As shown in Figure 2i, no obvious attenuation of the inner cavity pressure of the conformal adsorption unit was observed under low, medium and high negative pressure conditions, and the leakage rates within 120 s were 6.18 ± 0.05%, 6.38 ± 0.30%, 9.68 ± 0.04%, respectively. The above characterization demonstrated the superior adsorption capacity on various surfaces and reliable air tightness of the conformal adsorption unit, which provided critical support for the stable conformal attachment of BESS on human surfaces. The BESS maintained stable attachment during various wrist flexion activities (Figure S11, Supporting Information), confirming the potential mechanical adaptability of the system during daily activities. To evaluate skin compatibility, both BESS and a commercial adhesive patch were applied to the forearm for 5 min. Mild redness appeared at both sites upon removal, but the skin at the BESS site returned to normal within 3 min, while the chemical adhesive site took over 15 min to recover (Figure S12, Supporting Information). The skin is able to return to its normal state more quickly after the application of BESS. This is primarily due to the fact that BESS relies mainly on physical negative pressure to maintain adhesion, thereby avoiding allergic reactions that may be caused by chemical adhesives.

2.4. Characterization of the Vertical Pressure Loading Unit

In addition to enhancing the adsorption capacity, the octopus can regulate the pressure applied to the surface of the object by controlling the deformation of the internal protuberance of the sucker through muscles to realize free adsorption and separation. In order to realize the controllable pressure loading of BESS on the surface of the human body, a pneumatically controlled vertical pressure loading unit was designed. The inflatable structure is crucial in determining the capacity and efficiency of pressure loading. Based on the ellipsoidal internal protuberance, we designed ellipsoidal and bellows-shaped inflatable structures. Here, the digital force gauge was similarly used to verify the pressure loading capacity of the vertical pressure loading unit with different inflatable structures (**Figure 3**a,b). The pressure-sensing probe of the force gauge is brought into contact with the inflatable structure, ensuring that the pressure reading is zero. Then, the pneumatic control module is used to inflate the structure at a constant power. The internal air pressure and loading pressure variation curves for the bellows structure and the ellipsoidal structure are shown in Figure S13 (Supporting Information), respectively. The results indicated that the loading pressure increase rate and the maximum loading pressure of the bellows structure are significantly greater than those of the ellipsoidal structure. Figure 3c and Video S1 (Supporting Information) show the deformation of the two structures during the inflation process. Under different internal pressures, the vertical deformation of the bellows structure is noticeably greater than that of the ellipsoidal structure. Compared to the ellipsoidal structure, the bellows-shaped inflatable structure can provide vertical displacement through folding and expansion while reducing expansion in other directions. Additionally, its geometric shape helps to transmit pressure more effectively, thereby providing greater vertical loading pressure under the same air pressure.[42–44] The bellows structure demonstrated stable performance over 1000 repeated actuation cycles, confirming its mechanical durability for long-term use. The robustness is attributed to the strain-dispersing geometry of bellows and the superior resilience of the silicone material (Figure S14, Supporting Information).

In addition, the finite element analysis of the stress distribution of bellows-shaped and ellipsoidal inflatable structures under non-adsorbed and adsorbed states was also carried out (Figure 3d,e). Figure S15 (Supporting Information) shows the detailed stress distribution of the two inflatable structures for different internal air pressure conditions. It can be seen that as the internal air pressure of the inflatable structure increases, the bellows deform primarily along the major axis, while the ellipsoidal structure expands overall. And when adsorbed on the surface of an object, the internal stress of the bellows structure decreases significantly, indicating that the stress is effectively transferred to the surface of the object. Then, the maximum vertical loading pressure of the ellipsoidal and bellows-shaped inflatable structures was tested under different internal air pressure conditions in both non-adsorbed and adsorbed states (Figure 3f). The above simulation and experimental results indicated that the bellows-shaped inflatable structure is more suitable as a vertical pressure loading unit, offering more efficient and wider range vertical pressure loading capabilities. It is worth mentioning that when the internal air pressure reaches 90 kPa, the bellows-shaped inflatable structure can apply a vertical pressure of 5.62 N (≈16.23 kPa) on the adsorbed surface, which is sufficient to cover the pressure range applied during pulse palpation.

Additionally, we investigated the effect of the bellows size on its pressure capability and found that the amount of vertical pressure that can be applied is positively correlated with the diameter of the bellows (Figure 3g). Considering the miniaturization requirements of the device, a bellows structure with a diameter of 21 mm was ultimately chosen to construct the vertical pressure loading unit. Meanwhile, we also found that decreasing the initial distance between the bellows and the contact surface helps to increase the vertical loading pressure (Figure 3h). This is because when the bellows expands, a portion of the internal stress is used to maintain the deformation of the bellows structure. Under the condition of constant internal air pressure, reducing the distance between the contact surface and the bellows can limit the expansion deformation of the bellows, thus increasing the vertical loading pressure. It was also found that by increasing the modulus of the material at the top of the inflatable structure, the vertical loading pressure can be further improved. When

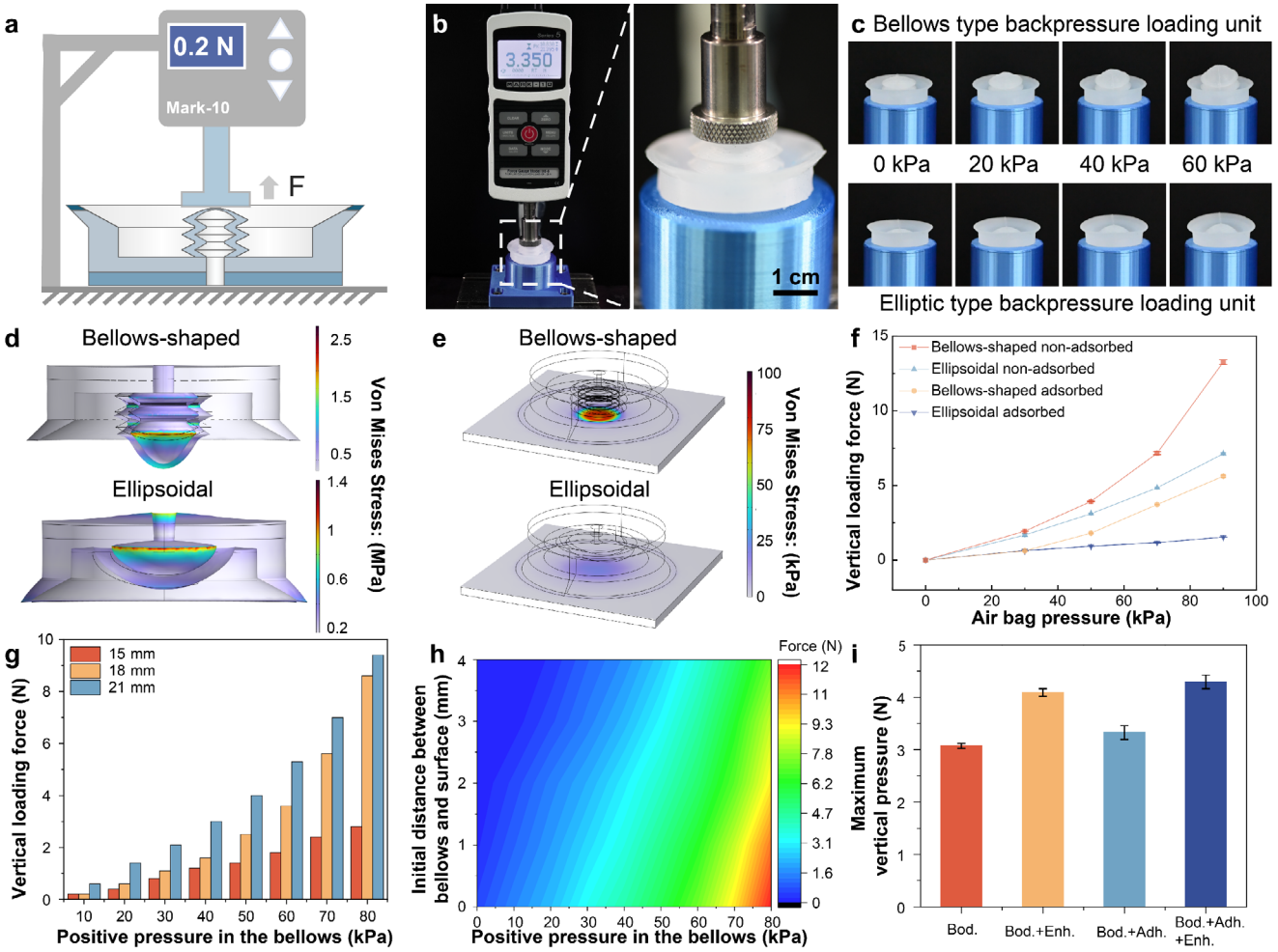

Figure 3. Characterization of the pressurization capacity of the vertical pressure loading unit. a) Schematic of the test method for vertical pressure loading capacity. b) Scenario of using the dynamometer to test the pressurization capacity. c) Comparison of bellows and ellipsoidal vertical pressure loading units expanding at 0–60 kpa. d) The finite element simulation of stress distribution in the bellows and ellipsoidal pressure loading unit was carried out at a constant air pressure of −90 kPa in the absence of adsorption. e) The finite element simulation of stress distribution on the bottom surface of the bellows and ellipsoidal pressure loading unit was conducted under adsorption at a constant air pressure of −90 kPa. f) Variation of loading pressure for bellows-shaped and ellipsoidal in adsorption (−50 kPa) and non-adsorption states. g) Effect of bellows diameter on pressurization capacity. Variation of pressurizing capacity with internal air pressure for different diameters of bellows-shaped vertical pressure loading unit in non-adsorbed state. h) Effect of initial distance between bellows structure and adsorption surface on pressurization capacity. i) Effect of adding an adhesion layer (Adh.) to a flexible body (Bod.) and adding a enhancement layer (Enh.) material on pressurization capacity. f, i: Data are presented as mean ± S.E.M. (n = 3 independent experiments). The error bars represent the precision of the mean estimate.

the internal air pressure is maintained at 60 kPa, the inflatable structure using PDMS as the pressure enhancement layer can increase the vertical pressure by ≈30% compared to the inflatable structure using soft materials (Dragon Skin) alone (Figure 3i). High-modulus materials reduce energy loss during the pressure loading process because they are more resistant to elastic deformation. This means that the internal air pressure can be more effectively converted into vertical pressure without dissipating due to material deformation. Furthermore, the adhesive layer helps the BESS conform to complex surfaces, facilitating the formation of a seal without affecting the applied vertical pressure. Through the above optimization, combined with the pneumatic control module, the vertical pressure loading unit can realize the controllable pressure loading on the contact surface under the adsorbed state, which endows BESS with the ability to pressurize the local human body accurately and efficiently. To further elucidate the mechanical coupling between suction adhesion and vertical pressure loading in the BESS, we analyzed the force equilibrium states under different levels of negative pressure. As shown in Figure S16 (Supporting Information), the BESS transitions from an initial suction state, in which the vacuum-induced force is balanced by the upward support from the skin, to a critical separation state. At this point, the vertical separation force generated by bellows inflation equals the suction force, and the skin no longer provides support. Therefore, the maximum suction force of the suction cup also limits the maximum vertical pressure that the bellows-shaped inflatable structure can apply. As shown in Figure S17 (Supporting Information), increasing the vacuum from −40

to −80 kPa led to an increase in vertical force output, rising from 3.42 to 4.59 N.

2.5. Characterization of the Pressure Sensing Unit

To effectively sense dynamic pressure signals from human pulses, a stress-enhanced piezoelectric pressure sensing unit was developed. When the PVDF sensing layer is subjected to an external force, the dipole moments within the molecular chains change due to deformation, leading to polarization on the material's surface and the accumulation of positive and negative charges on the two surfaces of the material. By connecting electrodes to the PVDF surface, these charges can be collected and converted into measurable electrical signals, enabling the detection of external pressure[45] (**Figure 4a**). The performance of the piezoelectric sensor is affected by the thickness of the piezoelectric layer and the substrate. Here, we tested the electrical output of sensors with combinations of three PVDF thicknesses (28, 52, and 110 μm) and three PI substrate thicknesses (125, 175, and 225 μm) (Figure 4b). Periodic pressure was applied using a linear motor (LinMot E1100), and the specific waveforms for open-circuit voltage, short-circuit current, and transferred charge of the sensors are shown in Figures S18–S20 (Supporting Information). The combination of 28 μm PVDF and 175 μm PI was found to exhibit ideal electrical performance. Subsequently, the output voltage under different pressures and the response time of the sensor for this combination were tested, as shown in Figure 4c and Figure S21 (Supporting Information), respectively. The results show that the piezoelectric sensor exhibits a typical two-stage linear relationship, with a sensitivity reaching 1.05 V/N over a wide pressure range, and a response time of up to 8.7 ms. The optical photograph of the piezoelectric sensor is shown in Figure 4d, with a diameter of 15 mm and an overall thickness of only 384 μm. In addition, 10000 consecutive working cycle tests have proved that the sensor has good stability and fatigue resistance (Figure 4e).

Pulse waves are the pressure waves generated by cardiac activity that cause the arterial walls to expand and transmit pressure to surrounding tissues and the skin's surface.[46,47] When placed above an artery, the piezoelectric sensor can directly convert the subtle pulse into electrical signals, thereby enabling the collection of pulse pressure signals[48] (Figure 4f). To achieve more effective detection of subtle pulse pressure signals, the surface of the PI substrate was etched to construct a micropillar array structure (Figure S22, Supporting Information), utilizing localized stress concentration to enhance the sensor's response to slight pressure signals. Through finite element analysis, the surface stress and potential distribution of the piezoelectric sensor with and without micropillar structure PI substrate under applied force were compared (Figure S23, Supporting Information and Figure 4g). The results indicate that when subjected to external forces, the stress concentrates around the micropillar structure, resulting in a greater surface potential difference. When actually used for pulse detection, the peak output voltage directly obtained by the piezoelectric sensor with the micropillar structure can reach 1.34 V, which is ≈2.6 times that of the sensor without structure (Figure 4h). Moreover, the pulse pressure and electrocardiogram (ECG) signals of the human body were synchronously collected by the prepared pressure sensing unit and a commercial ECG measuring instrument, as shown in Figure 4i,j. Here, a Poincaré plot is used to perform a statistical analysis of the peak intervals of the ECG signal (R-R intervals) and the pulse pressure signal (P-P intervals), which can be further used for heart rate variability analysis (Figure S24, Supporting Information).[49] Figure 4k shows a high linear correlation between the R-R intervals and the P-P intervals, with an R^2 value of 0.996. The findings demonstrate that the pressure sensing unit is capable of precise pulse detection, with the potential for medical-grade cardiovascular monitoring. To further assess waveform-level fidelity, we performed cross-correlation analysis across repeated trials from 17 individuals. As shown in Figure S25 (Supporting Information), the average waveform similarity remained consistently high between baseline and stress-modulated stages (mean fidelity ≈ 0.95), confirming that BESS captures reproducible and physiologically relevant pulse morphology suitable for downstream feature extraction and modeling.

2.6. Adaptive Pulse Monitoring System Based on BESS

The depth and intensity of pulse varies across arterial sites, and there can also be significant variations in pulses at the same site among different individuals. How to realize adaptive optimal pulse detection through self-adaptive bioinspired conformal perception across individuals and detection sites is a key challenge of current pulse sensing. Here, we constructed BESS by seamlessly integrating the conformal adsorption unit, the vertical pressure loading unit, and the pressure sensing unit, aiming to achieve stable, conformal attachment and controllable pressure loading in situ on the human body. To assess the pulse detection ability of the BESS across arterial sites, the BESS was placed over the superficial temporal artery, the brachial artery, and the radial artery, respectively. As shown in **Figure 5a**, through negative pressure adsorption, BESS could be easily attached to skin surfaces with different curvatures. By further adjusting the loading pressure, the pulse signals of the three arteries can be clearly captured (Figure 5b).

Additionally, combined with the pneumatic control module, signal acquisition and transmission module, an adaptive pulse monitoring system based on BESS was developed (Figure 5c). In the case of increasing external pressure, the dynamic characteristics of pulse wave amplitude increase first, until reaching the peak, and then decrease. This dynamic response can be quantitatively evaluated by three different parameters: V_{peak} describes the peak amplitude of the pulse wave under dynamic pressure, F_{peak} represents the contact pressure when the peak amplitude is reached, W_{pulse} is the range of contact pressure where the pulse amplitude remains above 80% of its peak[50] (Figure 5d). By utilizing the active pressurization and high-sensitivity pulse pressure-sensing capabilities of BESS, it is possible to effectively extract pulse amplitude dynamic response metrics during continuous pressurization, thereby enabling standardized pulse analysis via localized stress excitation. These metrics help to quantify traditional pulse diagnostic criteria, thereby improving the accuracy and applicability of pulse analysis in modern medical research.

To further explore the mechanisms behind the dynamic response of pulse wave amplitude, we used a hemodynamics-based

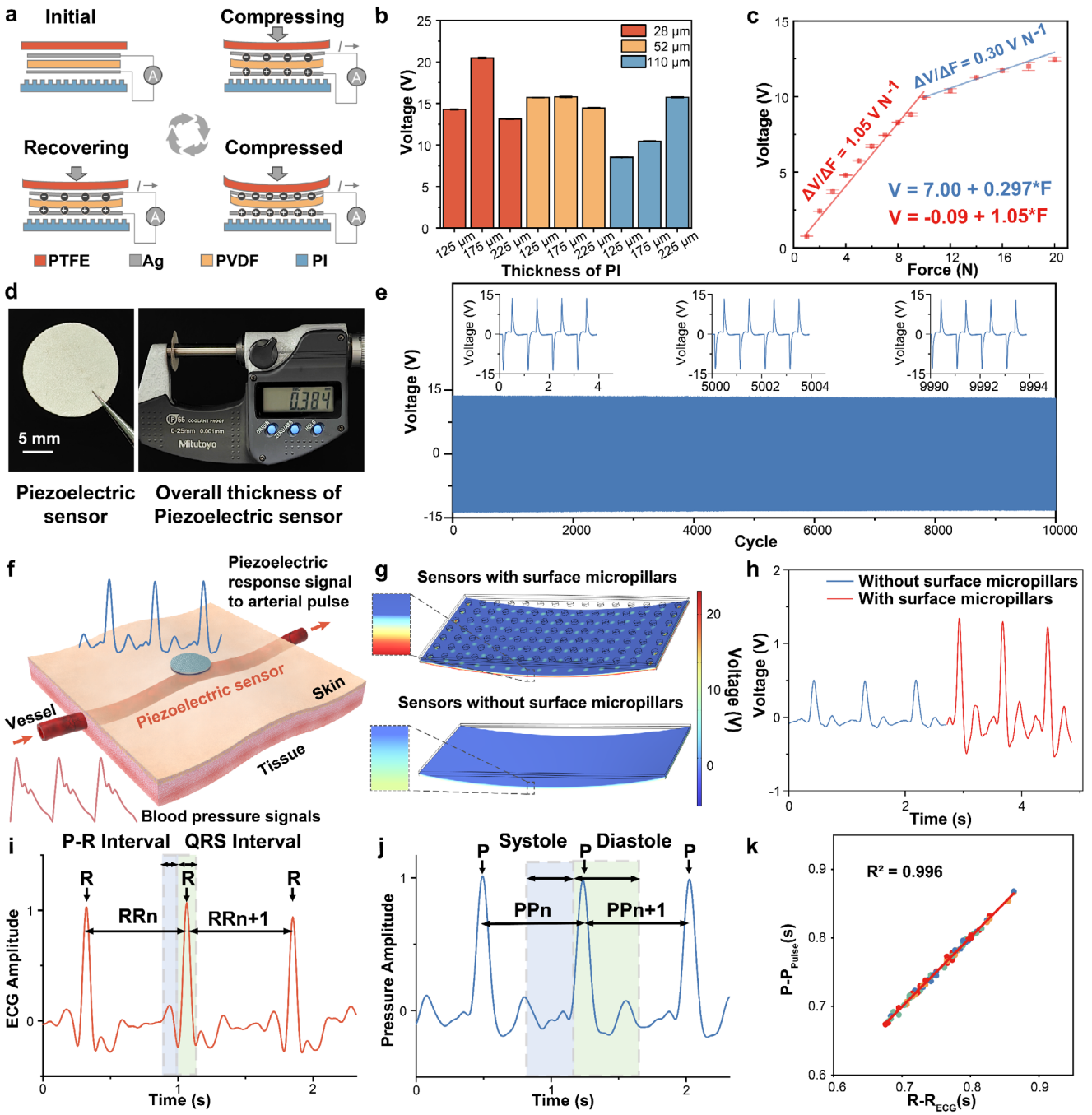

Figure 4. Performance characterization of the pressure sensing unit and demonstration of pulse detection capabilities. a) Working principle of the pressure sensing unit. b) Open-circuit voltage of the pressure sensing unit with the combination of different thicknesses of substrate and different thicknesses of PVDF. c) Voltage output of the pressure sensing unit at different pressures. d) Physical and overall thickness demonstration of piezoelectric sensors. e) Fatigue stability test for piezoelectric sensors. f) Piezoelectric sensors convert the mechanical signal of the pulse into an electrical signal schematically. g) Comparison of voltage distributions from finite element simulations with and without micropillar structures. h) Comparison of pressure sensing unit voltage output with and without ICP etching. i) Demonstration of the ECG signal measured by the ECG sensor. j) Demonstration of the pulse signal measured by the pressure sensing unit at the same time. k) By analyzing the R-R and P-P intervals, the linear relationship between the pulse signal acquired by the pressure sensing unit and the ECG signal is demonstrated. b,c: Data are presented as mean ± S.E.M. (n = 3 independent experiments). The error bars represent the precision of the mean estimate.

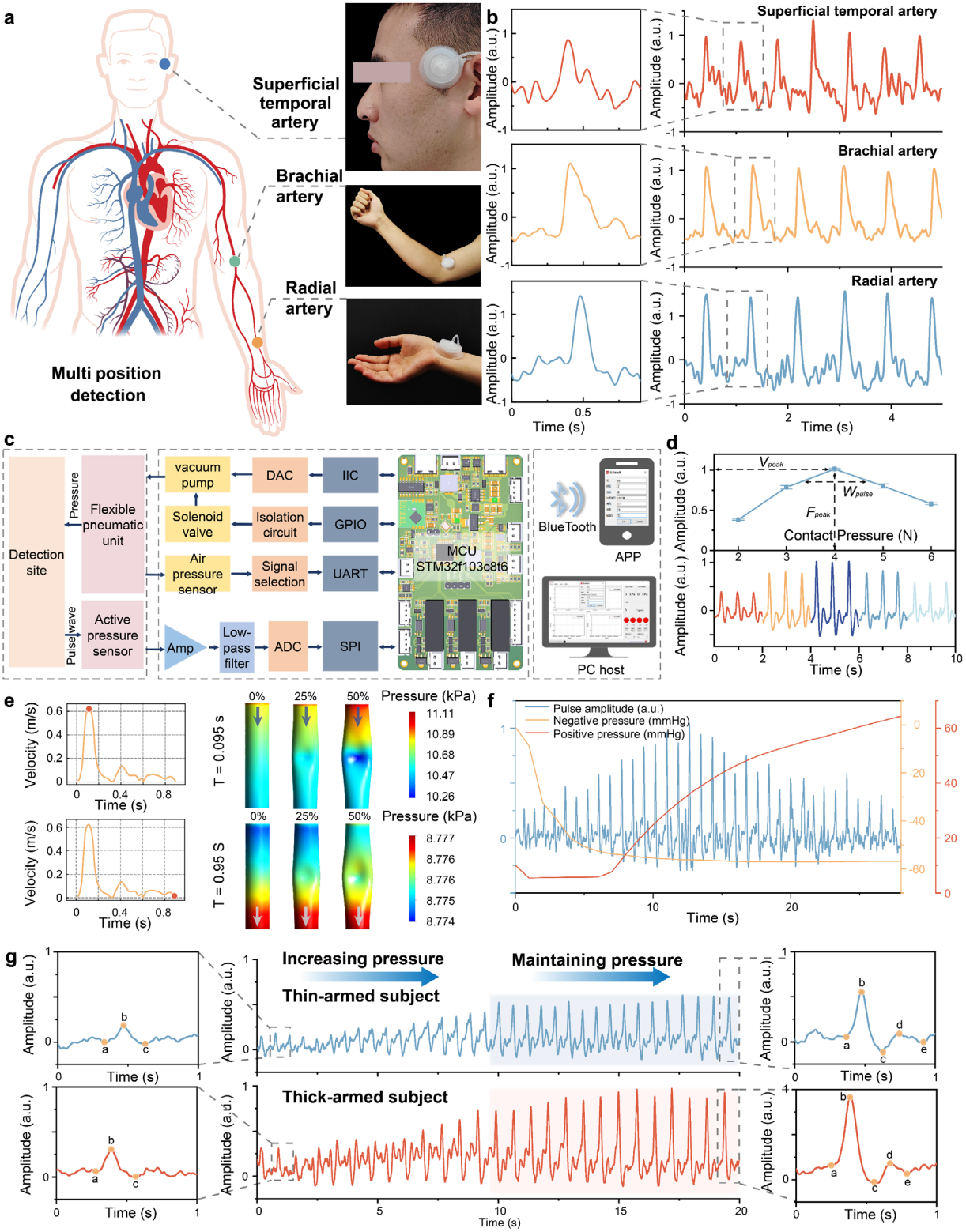

Figure 5. Performance evaluation of BESS cross-individual and regional pulse monitoring. a) Schematic of BESS for superficial temporal, brachial, and radial artery testing. b) Pulse waveforms at the superficial temporal, brachial, and radial arteries acquired by BESS. c) Block diagram of the hardware and software of the BESS-based adaptive pulse monitoring system. d) Dynamic response and quantification parameters of pulse amplitude under external pressure. e) Hemodynamic simulation of the pulse as external pressure increases. f) Dynamic response of BESS to pulse wave amplitude as pressure increases. g) Adaptive pulse detection for thick and thin arms using BESS. d: Data are presented as mean ± S.E.M. (n = 3 independent experiments). The error bars represent the precision of the mean estimate.

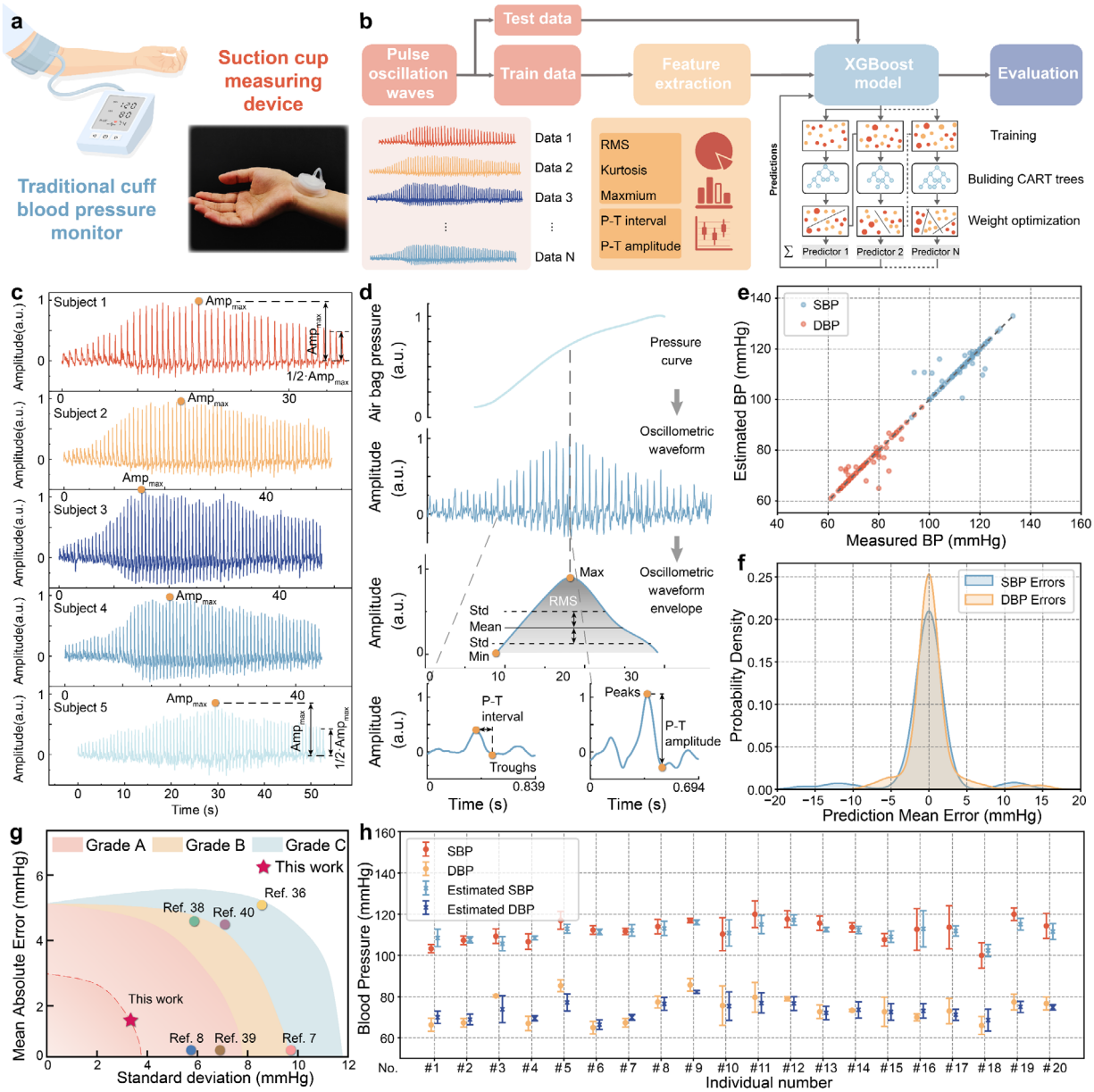

Figure 6. Establishment of a smart BP estimation model and performance evaluation of BESS for BP estimation. a) Traditional cuff BP monitor and smart BP estimation based on BESS. b) Flowchart of XGBoost-based BP model construction. c) Typical pulse oscillation wave captured by BESS. d) Schematic representation of the data processing and feature extraction process combining the classical oscillometric and pulse wave feature methods. e) Distribution of estimated and measured values for SBP and DBP for XGBoost-based BP estimation model. f) Probability density plots of SBP and DBP error distributions for XGBoost-based BP estimation models. g) Comparison of the accuracy of XGBoost-based BP estimation model with other partial work in assessing SBP. h) Distribution of estimated and measured SBP and DBP values for 20 subject individuals. h: Data are presented as mean ± S.E.M. (n = 3 independent experiments). The error bars represent the precision of the mean estimate.

method to simulate and try to explain this phenomenon (Note S1, Supporting Information). Figure 5e illustrates the stress distribution in a blood vessel under different deformations at the maximum and minimum blood flow velocities within a pulse cycle. According to the simulation results, we can infer that the applied local pressure causes changes in the local geometry of the blood vessel, which in turn leads to corresponding changes in upstream and downstream pressures. This is reflected in a stronger pulse, with the sensor measuring an increased amplitude of the pulse wave. Furthermore, varying levels of external pressure were applied to the brachial artery of a 28-year-old healthy female subject, with real-time vascular deformation monitored via ultrasonography (Figure S26, Supporting Information). The results indicate that as the external pressure increases, the diameter of the blood vessels gradually decreases, leading to corresponding hemodynamic changes. This direct vascular deformation under controlled pressure supports the physiological basis of pulse amplitude modulation captured by the BESS.

When using the adaptive pulse monitoring system based on BESS for pulse detection, stable negative pressure adsorption of BESS at the arterial site is first achieved through pneumatic control. Subsequently, vertical pressure is applied by inflating the airbag while capturing the corresponding pulse wave signals. As the positive pressure gradually increases, the amplitude of the pulse wave first increases to a peak and then gradually decreases, as shown in Figure 5f. Record the positive pressure corresponding to the peak of the pulse amplitude and use it as the optimal pulse detection pressure. Then, through program control, pressure is reapplied to this optimal pulse detection pressure and maintained to achieve adaptive pulse optimization monitoring. Due to individual differences in the intensity and depth of the pulse, the rate of increase in the amplitude of the pulse wave and the maximum peak value that can be achieved also vary during the pressurization process. To evaluate the cross-individual adaptive pulse monitoring capability of BESS, a comparative test was conducted with a thick-armed subject (a healthy 27-year-old male) and a thin-armed subject (a healthy 24-year-old female). As shown in Figure 5g, through adaptive pressurization, the amplitude of the pulse wave was significantly enhanced (approximately three-fold), and the number of characteristic points in the pulse wave increased, providing high-quality pulse signals for further diagnostic analysis. To evaluate the effectiveness of adaptive stress modulation, we assessed both intra-subject signal consistency and pulse amplitude enhancement. As shown in Figure S27a (Supporting Information), waveform overlays from three repeated measurements on the same participant exhibited broadly consistent morphology with minimal variation, suggesting reliable intra-subject repeatability under standardized conditions. In addition, the application of vertical loading led to notable increases in pulse amplitude and signal-to-noise ratio (SNR). A representative case is presented in Figure S27b (Supporting Information), while the group-level results from 13 participants are summarized in Figure S27c (Supporting Information), demonstrating a consistent trend of enhanced signal clarity under stress modulation.

2.7. Smart Blood Pressure Estimation System Based on BESS

As a vital physiological indicator of the human body, BP is closely related to pulse signals. Compared to traditional cuff-based BP measurements, the methods utilizing pulse wave ana lysis offer more convenience and comfort. Nevertheless, they still face critical issues, including limited generalization capability and insufficient interpretability.[6,51,52] Leveraging the localized dynamic pressurization and precise pulse monitoring capabilities of BESS, we have further developed a compact, accessible, and smart BP estimation system based on BESS (**Figure 6a**). Figure 6b illustrates the process of constructing the BP estimation model using machine learning. The model is trained using signal features extracted from pulse oscillation waves collected from different individuals based on BESS. After preprocessing the pulse oscillation waveforms, the most relevant features—comprising both overall features (e.g., root mean square, kurtosis, and maximum) and single pulse wave features (e.g., peak to trough interval (P-T interval) and peak to trough amplitude (P-T amplitude))—are selected as input for the BP estimation model. Here, the eXtreme Gradient Boosting (XGBoost) algorithm was chosen for model construction, which minimizes the loss function by iteratively updating the gradient to build the Classification And Regression Tree (CART). The ability to model complex nonlinear relationships between features makes it possible to establish the association between complex variations in pulse waves and BP under different pressure conditions, enabling the model to accurately estimate SBP/DBP. To standardize the acquisition of pulse oscillation waves, pulse signals are continuously collected during the pressure increase process. When the pulse amplitude reaches its maximum, it is recorded as $\mathbf{Amp}_{\mathbf{max}}$. The collection is completed when the pressure is further increased until the pulse amplitude decreases to half of the maximum amplitude. To facilitate model training, the normalization method is used to preprocess the acquired pulse oscillation waves.

Figure 6c displays some typical pulse oscillation waveforms from different subjects after normalization processing. Due to individual differences, the pulse oscillation waves collected from different subjects are not identical, mainly reflected in the rate of change of pulse amplitude and the maximum pulse amplitude. Figure 6d demonstrates the key steps in feature extraction from pulse oscillation waves in the BESS-based BP estimation system. Initially, a Gaussian envelope is used to extract the overall features of the oscillation wave. The extracted features include minimum, maximum, mean, standard deviation, root mean square, skewness, and kurtosis. These features reflect the statistical distribution, energy magnitude, symmetry, and shape characteristics of the pulse oscillation wave. Such overall features can indicate global changes in BP regulation, such as vascular compliance, pressure transmission efficiency, and peripheral resistance factors. For a single pulse waveform, the primary extracted features include the peak-trough interval (P-T interval) and peak-trough amplitude (P-T amplitude). The P-T interval characterizes the temporal spacing within each pressure oscillation cycle, reflecting vascular compliance, local arterial stiffness, and cardiac cycle dynamics under externally modulated pressure. The P-T amplitude represents the pressure fluctuation magnitude, indirectly reflecting the vascular elasticity and the strength of left ventricular ejection. Additionally, extracting the spectral entropy features of the pulse signal can reflect the complexity and energy distribution of the pulse oscillation wave in the frequency domain. These features capture subtle changes in the pulse wave from both time and frequency domain perspectives, providing richer and more detailed information. To evaluate intra-subject repeatability, repeated pulse measurements were performed on 10 subjects at the same anatomical location. Representative waveforms from a single subject across three trials demonstrated high morphological consistency (Figure S28a, Supporting Information). Corresponding extracted features showed low coefficient of variation (CV) values (Figure S28b, Supporting Information). Across all 10 subjects, the mean CVs for 10 selected features ranged from 12.3% to 21.5%, confirming stable signal characteristics for reliable machine learning-based BP estimation (Figure S28c, Supporting Information). Combining the overall features of pulse oscillation waves with the features of individual pulse waves allows for associating with BP at different levels. Overall features primarily reflect the trend of changes in vascular pressure, while individual pulse wave features capture dynamic blood

flow characteristics. The XGBoost algorithm can effectively correlate these features with BP (the importance of different features in this correlation process is shown in the feature importance plot; Figure S29, Supporting Information). This multidimensional feature analysis enables the BESS-based BP estimation system to incorporate both global and local information, significantly improving the model's accuracy and applicability.

BP values and corresponding pulse oscillation waves were collected from twenty-five volunteers at different times using a cuff sphygmomanometer and BESS, respectively, of which 80% was used as the model training set and 20% as the test set. Figure 6e shows the scatter plot of the model's estimated values for SBP and DBP against the actual BP measurements. The data points are primarily distributed along the diagonal dashed line, demonstrating the high accuracy of the constructed model. Figure 6f shows the probability density distribution of the mean error for the estimated values of SBP and DBP, with over 90% of the mean errors falling within the range of ±5 mmHg. Figure 6g and Figure S30 (Supporting Information) compare the performance of the BESS-based BP estimation with other BP estimation methods from previous studies in terms of SBP and DBP. The results indicate that the constructed model demonstrates superior accuracy, with an SBP estimation error of 1.36 mmHg ± 3.81 mmHg and a DBP estimation error of 1.15 mmHg ± 2.94 mmHg, meeting the Grade A of British Hypertension Society (BHS) standard.[53–57] Video S2 (Supporting Information) provides a detailed comparison of the entire process of BP detection using the BESS-based BP estimation system and a commercial cuff-based sphygmomanometer. To further assess the cross-individual detection ability of the model, the BESS-based BP estimation system was used to perform three BP estimations on twenty participants, and the results were compared with cuff-based measurements, as shown in Figure 6h. Both SBP and DBP estimations exhibit good consistency with the cuff-based measurements, demonstrating excellent cross-individual adaptability of the system. Table S2 (Supporting Information) provides a comprehensive comparison of BESS with representative wearable BP-monitoring systems and commercial products. Compared to other systems, BESS has a soft skin sucker design with negative pressure based attachment, enabling repeatable and conformal adhesion. It uniquely integrates oscillometry with pulse feature analysis methods to extract rich multi-dimensional waveform information. Unlike conventional cuff-based arterial occlusive systems, BESS operates in a non-arterial occlusive manner, offering high-precision blood pressure estimation while balancing comfort and ease of operation.

3. Conclusion and Discussion

Serving as vital noninvasive physiological signals, pulse and BP play a pivotal role in personalized cardiovascular health monitoring, as well as in the prevention and management of CVDs. Physiological differences among individuals, including factors such as skin curvature, wrist circumference, and fat layer thickness, contribute to the challenges in achieving applicable standardized pulse detection and analysis in existing monitoring technologies. For BP monitoring, while traditional cuff-based measurement methods, such as auscultation and oscillometry, inherently cause compressive discomfort, emerging cuff-less pulse wave analysis technologies exhibit limitations in accuracy across individuals and clinical interpretability. Breaking through the technical integration paradigm that features high accuracy, strong applicability, user-friendly portability, and clinical interpretability has become the bottleneck in the development of current personalized cardiovascular monitoring technologies.

Inspired by the mechanics of octopus suckers and the TCM pulse palpation, we have organically combined flexible sensing technology with flexible actuation technology to develop a biomimetic epidermal sensing sucker (BESS). An adaptive pulse sensing strategy was demonstrated, effectively enhancing the intensity of weak pulse signals by approximately three times. By utilizing the BESS for the in situ excitation and capture of pulse oscillation waves, we further established an interpretable high-accuracy blood pressure estimation model, with 1.36 ± 3.81 mmHg for SBP and 1.15 ± 2.94 mmHg for DBP, which meet the BHS Grade A standard. Specifically, three advancements beyond conventional approaches support these demonstrated capabilities: i) self-adaptive bioinspired conformal perception: by mimicking the negative pressure adsorption and active pressurization mechanism of octopus suction cups, BESS can provide stable attachment and conformal sensing to different arterial sites, along with controllable pressure loading in situ; ii) standardized pulse analysis via stress excitation: drawing on the pulse diagnosis of TCM, BESS successfully captures the pulse oscillation wave by applying increasing vertical pressure to the epidermis to cause stress excitation of local arterial blood vessels and blood flow; iii) innovative cuffless BP estimation system: a novel cuffless BP estimation system based on BESS has been developed, which integrates classical oscillometry with pulse wave features analysis through multidimensional data processing strategy. Combining biomimetic sensing strategies, traditional medicine, and artificial intelligence, we have provided a promising solution for personalized cardiovascular health monitoring. BESS boasts advantages such as flexibility, compactness, and user-friendliness, enabling efficient optimal pulse pressure signal acquisition. Furthermore, owing to the capacity to achieve high-accuracy BP estimation without obstructing arterial blood flow, BESS exhibits superior adaptability for individuals with stress intolerance or local injuries. A miniaturization roadmap has been proposed to guide the integration of pneumatic actuation, signal acquisition, circuit control, and wireless communication into a unified soft patch. This strategy envisions embedding compact micro-pumps and flexible circuits within the suction cavity, supported by soft encapsulation for skin conformability. The conceptual pathway toward full wearable integration is illustrated in Figure S31 (Supporting Information). The further integration and miniaturization of the system, along with the expansion of the training dataset and the enhancement of the algorithmic models, are expected to advance the application of BESS in long-term, precise, and personalized cardiovascular health care within both home-based and clinical settings.

4. Experimental Section

Fabrication of Biomimetic Adaptive Pressure Module: The fabrication process could be divided into three steps: 1) Design the shape and dimensions of the mold for the biomimetic pressure units (The structure is shown in Figure S32, Supporting Information) in 3D computer-aided

design software (SOLIDWORKS 2021), and then fabricate the mold using Fused Deposition Modelling 3D printing technology. 2) Dragon Skin (30, Smooth-On) was poured into the mold and then left at 23 °C for ≈16 h to cure and then removed from the mold. 3) A layer of PDMS (Sylgard 184 silicone elastomer, 10:1) was added to the top of the Dragon Skin at a thickness of ≈2 mm, and finally, a layer of SkinTite (Smooth-On) was applied to the funnel-shaped edge layer, and left at 23 °C for ≈5 min to finish curing.

Fabrication of Arterial Pulse Pressure Sensing Module: First, a double-sided silver-coated PVDF film (TE Connectivity) was cut into circles of 15 mm diameter, and silver paste was used to secure the wires at both ends of the PVDF film. Subsequently, a PI film (DuPont) with a thickness of 175 µm and a PTFE film (ASF-110FR, Chukoh Chemical Co., Ltd.) with a thickness of 8 µm, both of the same size, were cut. Finally, the PVDF membrane was first bonded to the PI membrane by adhesive bonding, and then the PTFE was bonded to it by adhesive bonding.

The fabricated nanostructured PI film was processed by an ICP etching system (SENTECH, SI 500). A piece of 175 µm PI film was rinsed with menthol, isopropyl alcohol, and deionized water. Subsequently, a 10 nm thick Au was sputtered onto the PI surface, which acted as the mask for the etching process. Finally, this PI was etched through the ICP reactive ion etching for 180 s. The reaction gas was 15.0 sccm Ar, 10.0 sccm O_2, and 30.0 sccm CF_4 in the ICP process. The upper and lower powers of the ICP are 400 and 100 W, respectively.

Characterization: A multi-channel oscilloscope (Teledyne LeCroy, HD4096) and an electrostatic meter (Keithley, 6517B) were used to record the sampling of electrically relevant data such as voltages, currents, and charge transfers at a constant sampling frequency of 1000 Hz. The movement of the test material was controlled using linear motors (LinMot, E1100), which enabled the loading displacement and loading speed to be Precise control of loading displacement and loading speed was realized. Uniaxial tensile tests were performed using a motorized vertical test stand (Mark-10, ESM301) and real-time tensile forces were detected using a force gauge (Mark 10, ESM301). The morphology after PI etching was observed using a heliostat emission scanning electron microscope (Hitachi, SU8020). The potential distribution of the arterial pulse pressure sensing module under bending was analyzed by COMSOL Multiphysics finite element simulation. A digital camera (SONY, ILCE-7M3) was used to take photographs of the morphological changes of the airbag at a recorded frame rate of 100 frames per second.

Analysis of the Blood Flow After Compression: The alternative of blood flow pattern induced by compression was simulated by Ansys 19.0 (Ansys Inc., Canonsburg, PA) software. This compression is simplified as deformation under a fixed displacement, and the corresponding induced compression was calculated. The information of modeling and computational setup is provided in the additional materials.

Volunteer Data Acquisition: For the HRV test, an ECG sensor (TI., ADS1293) and a pressure transducer were used to simultaneously test a 26-year-old healthy volunteer. The participant was asked to remain in an upright sitting position with ECG electrodes attached and an arterial pulse pressure sensing module placed at the radial artery. The subject was allowed to rest for 5 min before the data acquisition process. The subject's ECG and pulse signals were recorded at a sampling rate of 256 and 1000 Hz, and then kept at rest for 1 min. For the BP test, volunteers of different ages and genders were selected to participate in the experiment. Volunteers were asked to maintain an upright sitting position and rest for 5 min. Then the BESS was adsorbed at the radial artery to start the test, and the pulse signal was recorded at a sampling rate of 1000 Hz and transferred to a machine learning model for BP estimation. Then, a cuff-based sphygmomanometer (Raycome Health Technology Co., Ltd, BP550B-H) was worn on the same arm after 5 min of rest.

The human participants in the experiments provided the informed signed consent. The wearable experiments were approved by the Committee on Ethics of the Beijing Institute of Nanoenergy and Nanosystems (Approval No. 2023002LZ).

Statistical Analysis: The statistical analysis was performed on data from at least three independent samples, and results were presented as mean ± standard error of the mean(S.E.M.). The differences between the two groups were analyzed by an unpaired Student's *t* test. The data used for machine learning were preprocessed using normalization and processed using PyCharm (PyCharm Community Edition 2021, JetBrains s.r.o., Czech Republic) software. The rest of the data were analyzed using Origin (OriginPro 2021, OriginLab Corporation, USA) for data analysis. $p < 0.01$, $p < 0.001$ were considered statistically significant.

Supporting Information

Supporting Information is available from the Wiley Online Library or from the author.

Acknowledgements

This work was supported by the National Key Research and Development Program of China (2022YFB3804700), the National Natural Science Foundation of China (82202075, T2125003), the Natural Science Foundation of Beijing Municipality (L245015, Z240022), the National Postdoctoral Program for Innovative Talent (BX20220380), the China Postdoctoral Science Foundation (2022M710389), and the Fundamental Research Funds for the Central Universities.

Conflict of Interest

The authors declare no conflict of interest.

Data Availability Statement

The data that support the findings of this study are available from the corresponding author upon reasonable request.

Keywords

biomimetic sucker, cardiovascular monitoring, machine learning, stress excitation

Received: July 8, 2025
Revised: September 8, 2025
Published online:

[1] E. J. Benjamin, P. Muntner, A. Alonso, M. S. Bittencourt, C. W. Callaway, A. P. Carson, A. M. Chamberlain, A. R. Chang, S. Cheng, S. R. Das, F. N. Delling, L. Djousse, M. S. V. Elkind, J. F. Ferguson, M. Fornage, L. C. Jordan, S. S. Khan, B. M. Kissela, K. L. Knutson, T. W. Kwan, D. T. Lackland, T. T. Lewis, J. H. Lichtman, C. T. Longenecker, M. S. Loop, P. L. Lutsey, S. S. Martin, K. Matsushita, A. E. Moran, M. E. Mussolino, et al., *Circulation* **2019**, *139*, 2735.

[2] A. Timmis, N. Townsend, C. P. Gale, A. Torbica, M. Lettino, S. E. Petersen, E. A. Mossialos, A. P. Maggioni, D. Kazakiewicz, H. T. May, D. De Smedt, M. Flather, L. Zuhlke, J. F. Beltrame, R. Huculeci, L. Tavazzi, G. Hindricks, J. Bax, B. Casadei, S. Achenbach, L. Wright, P. Vardas, L. Mimoza, G. Artan, D. Aurel, M. Chettibi, N. Hammoudi, H. Sisakian, S. Pepoyan, B. Metzler, et al., *Eur. Heart J.* **2019**, *41*, 12.

[3] B. Cannon, *Nature* **2013**, *493*, S2.

[4] K. Meng, X. Xiao, W. Wei, G. Chen, A. Nashalian, S. Shen, X. Xiao, J. Chen, *Adv. Mater.* **2022**, *34*, 2109357.

[5] H. U. Chung, B. H. Kim, J. Y. Lee, J. Lee, Z. Xie, E. M. Ibler, K. Lee, A. Banks, J. Y. Jeong, J. Kim, C. Ogle, D. Grande, Y. Yu, H. Jang, P. Assem, D. Ryu, J. W. Kwak, M. Namkoong, J. B. Park, Y. Lee, D. H. Kim, A. Ryu, J. Jeong, K. You, B. Ji, Z. Liu, Q. Huo, X. Feng, Y. Deng, Y. Xu, et al., *Science* **2019**, *363*, aau0780.

[6] J. Li, H. Jia, J. Zhou, X. Huang, L. Xu, S. Jia, Z. Gao, K. Yao, D. Li, B. Zhang, Y. Liu, Y. Huang, Y. Hu, G. Zhao, Z. Xu, J. Li, C. K. Yiu, Y. Gao, M. Wu, Y. Jiao, Q. Zhang, X. Tai, R. H. Chan, Y. Zhang, X. Ma, X. Yu, *Nat. Commun.* **2023**, *14*, 5009.
[7] S. Li, H. Wang, W. Ma, L. Qiu, K. Xia, Y. Zhang, H. Lu, M. Zhu, X. Liang, X.-E. Wu, H. Liang, Y. Zhang, *Sci. Adv.* **2023**, *9*, adh0615.
[8] F. Wang, P. Jin, Y. Feng, J. Fu, P. Wang, X. Liu, Y. Zhang, Y. Ma, Y. Yang, A. Yang, X. Feng, *Sci. Adv.* **2021**, *7*, abi9283.
[9] M. Deng, C. Du, J. Fang, C. Xu, C. Guo, J. Huang, K. Li, L. Chen, Y.-T. Zhang, Y. Chang, T. Pan, *npj Flexible Electron.* **2024**, *8*, 45.
[10] J. Luo, J. Wu, X. Zheng, H. Xiong, L. Lin, C. Liu, H. Liu, H. Tang, H. Liu, F. Han, Z. Liu, Z. Deng, C. Liu, T. Cui, B. Li, T.-L. Ren, J. Zhou, Y. Qiao, *Nano Res.* **2024**, *17*, 10058.
[11] R. Velik, *Eur. J. Integr. Med.* **2015**, *7*, 321.
[12] X. Wang, G. Wu, X. Zhang, F. Lv, Z. Yang, X. Nan, Z. Zhang, C. Xue, H. Cheng, L. Gao, *Adv. Mater.* **2025**, *37*, 2410312.
[13] W. Chen, X. Wang, J. Chen, et al., in *IoT as a Service* (Eds: B. Li, C. Li, M. Yang, Z. Yan, J. Zheng), Springer International Publishing, Cham **2021**, pp. 336–346.
[14] Y. Fu, S. Zhao, R. Zhu, *IEEE Trans. Biomed. Eng.* **2019**, *66*, 1412.
[15] R. M. Carey, P. Muntner, H. B. Bosworth, P. K. Whelton, *J. Am. Coll. Cardiol.* **2018**, *72*, 1278.
[16] K. Kario, *Hypertension* **2020**, *76*, 640.
[17] A. Kumar, R. Anel, E. Bunnell, K. Habet, S. Zanotti, S. Marshall, A. Neumann, A. Ali, M. Cheang, C. Kavinsky, J. E. Parrillo, *Crit. Care Med.* **2004**, *32*, 691.
[18] S. Gong, L. W. Yap, Y. Zhang, J. He, J. Yin, F. Marzbanrad, D. M. Kaye, W. Cheng, *Biosens. Bioelectron.* **2022**, *205*, 114072.
[19] D. Kireev, K. Sel, B. Ibrahim, N. Kumar, A. Akbari, R. Jafari, D. Akinwande, *Nat. Nanotechnol.* **2022**, *17*, 864.
[20] D. Franklin, A. Tzavelis, J. Y. Lee, H. U. Chung, J. Trueb, H. Arafa, S. S. Kwak, I. Huang, Y. Liu, M. Rathod, J. Wu, H. Liu, C. Wu, J. A. Pandit, F. S. Ahmad, P. M. McCarthy, J. A. Rogers, *Nat. Biomed. Eng.* **2023**, *7*, 1229.
[21] C. Wang, X. Li, H. Hu, L. Zhang, Z. Huang, M. Lin, Z. Zhang, Z. Yin, B. Huang, H. Gong, S. Bhaskaran, Y. Gu, M. Makihata, Y. Guo, Y. Lei, Y. Chen, C. Wang, Y. Li, T. Zhang, Z. Chen, A. P. Pisano, L. Zhang, Q. Zhou, S. Xu, *Nat. Biomed. Eng.* **2018**, *2*, 687.
[22] S. Zhou, G. Park, K. Longardner, M. Lin, B. Qi, X. Yang, X. Gao, H. Huang, X. Chen, Y. Bian, H. Hu, R. S. Wu, W. Yue, M. Li, C. Lu, R. Wang, S. Qin, E. Tasali, T. Karrison, I. Thomas, B. Smarr, E. B. Kistler, B. A. Khiami, I. Litvan, S. Xu, *Nat. Biomed. Eng.* **2024**, *9*, 865.
[23] Y. L. Shevchenko, J. E. Tsitlik, *Circulation* **1996**, *94*, 116.
[24] U. Tholl, K. Forstner, M. Anlauf, *Nephrol., Dial., Transplant.* **2004**, *19*, 766.
[25] J. Jilek, T. Fukushima, *Biomed. Instrum. Technol.* **2005**, *39*, 237.
[26] B. S. Alpert, D. Quinn, D. Gallick, *J. Am. Soc. Hypertension* **2014**, *8*, 930.
[27] S. Li, H. Wang, W. Ma, L. Qiu, K. Xia, Y. Zhang, H. Lu, M. Zhu, X. Liang, X.-E. Wu, H. Liang, Y. Zhang, *Sci. Adv.* **2023**, *9*, adh0615.
[28] T. Zhang, N. Liu, J. Xu, Z. Liu, Y. Zhou, Y. Yang, S. Li, Y. Huang, S. Jiang, *Innovation* **2023**, *4*, 100485.
[29] Y. Wu, X. Li, H. Tian, D. Wang, J. Zhang, L. Wang, J. Shao, *Adv. Funct. Mater.* **2023**, *33*, 2210562.
[30] M. Wu, X. Zheng, R. Liu, N. Hou, W. H. Afridi, R. H. Afridi, X. Guo, J. Wu, C. Wang, G. Xie, *Adv. Sci.* **2022**, *9*, 2104382.
[31] S. Baik, H. J. Lee, D. W. Kim, H. Min, C. Pang, *ACS Appl. Mater. Interfaces* **2019**, *11*, 25674.
[32] N. N. Ahmad, N. N. N. Ghazali, A. T. A. Rani, C. C. Kee, Y. H. Wong, *Mater. Sci. Semicond. Process.* **2023**, *166*, 107731.
[33] Z. Zhu, J. Wang, X. Pei, J. Chen, X. Wei, Y. Liu, P. Xia, Q. Wan, Z. Gu, Y. He, *Sci. Adv.* **2023**, *9*, adh2213.
[34] A. A. Alsharif, A. M. Syed, X. Li, N. A. Alsharif, G. Lubineau, N. El-Atab, *Adv. Funct. Mater.* **2024**, *34*, 2406341.
[35] W. Li, Y. Yu, R. Huang, X. Wang, P. Lai, K. Chen, L. Shang, Y. Zhao, *Adv. Sci.* **2023**, *10*, 2301479.
[36] H. J. Lee, S. Baik, G. W. Hwang, J. H. Song, D. W. Kim, B.-Y. Park, H. Min, J. K. Kim, J.-S. Koh, T.-H. Yang, C. Pang, *ACS Nano* **2021**, *15*, 14137.
[37] Y. Zou, P. Tan, B. Shi, H. Ouyang, D. Jiang, Z. Liu, H. Li, M. Yu, C. Wang, X. Qu, L. Zhao, Y. Fan, Z. L. Wang, Z. Li, *Nat. Commun.* **2019**, *10*, 2695.
[38] S. Baik, D. W. Kim, Y. Park, T.-J. Lee, S. Ho Bhang, C. Pang, *Nature* **2017**, *546*, 396.
[39] S. Mallick, Z. Ahmad, K. W. Qadir, A. Rehman, R. A. Shakoor, F. Touati, S. A. Al-Muhtaseb, *Ceram. Int.* **2020**, *46*, 2949.
[40] A. Al-Saygh, D. Ponnamma, M. AlMaadeed, P. Vijayan P, A. Karim, M. Hassan, *Polymers* **2017**, *9*, 33.
[41] X. Chen, Y. Luo, Y. Chen, S. Li, S. Deng, B. Wang, Q. Zhang, X. Li, X. Li, C. Wang, J. He, H. Tian, J. Shao, *Adv. Sci.* **2024**, *11*, 2408082.
[42] R. Hashem, M. Stommel, L. K. Cheng, W. Xu, *IEEE/ASME Trans. Mechatron.* **2021**, *26*, 2327.
[43] R. Balak, Y. C. Mazumdar, presented at *2020 IEEE/RSJ International Conference on Intelligent Robots and Systems (IROS)*, Las Vegas, NV, USA, January **2020**, pp. 8673–8679.
[44] G. Dämmer, S. Gablenz, A. Hildebrandt, Z. Major, *Front. Rob. AI* **2019**, *6*, 34.
[45] Y. Zou, L. Bo, Z. Li, *Fundam. Res.* **2021**, *1*, 364.
[46] J.-J. Wang, A. B. O'Brien, N. G. Shrive, K. H. Parker, J. V. Tyberg, *Am. J. Physiol.: Heart Circ. Physiol.* **2003**, *284*, H1358.
[47] Z. Alizadeh Sani, A. Shalbaf, H. Behnam, R. Shalbaf, *J. Digital Imag.* **2015**, *28*, 91.
[48] Q. Zheng, B. Shi, Z. Li, Z. L. Wang, *Adv. Sci.* **2017**, *4*, 1700029.
[49] X.-L. Yang, G.-Z. Liu, Y.-H. Tong, H. Yan, Z. Xu, Q. Chen, X. Liu, H.-H. Zhang, H.-B. Wang, S.-H. Tan, *J. Geriatr. Cardiol.* **2015**, *12*, 448.
[50] C.-C. Tyan, S.-H. Liu, J.-Y. Chen, J.-J. Chen, W.-M. Liang, *IEEE Trans. Biomed. Eng.* **2008**, *55*, 288.
[51] Z. Yi, Z. Liu, W. Li, T. Ruan, X. Chen, J. Liu, B. Yang, W. Zhang, *Adv. Mater.* **2022**, *34*, 2110291.
[52] P. Tan, Y. Xi, S. Chao, D. Jiang, Z. Liu, Y. Fan, Z. Li, *Biosensors* **2022**, *12*, 234.
[53] R. He, Z.-P. Huang, L.-Y. Ji, J.-K. Wu, H. Li, Z.-Q. Zhang, presented at 2016 IEEE 13th International Conference on Wearable and Implantable Body Sensor Networks (BSN), San Francisco, CA, USA, June **2016**, pp. 194–198.
[54] E. O'Brien, J. Petrie, W. Littler, M. de Swiet, P. L. Padfield, K. O'Malley, M. Jamieson, D. Altman, M. Bland, N. Atkins, *J. Hypertens.* **1990**, *8*, 607.
[55] S. Yang, Y. Zhang, S.-Y. Cho, R. Correia, S. P. Morgan, *Opt. Quantum Electron.* **2021**, *53*, 93.
[56] B. Ibrahim, R. Jafari, *Sci. Rep.* **2022**, *12*, 319.
[57] K. Duan, Z. Qian, M. Atef, G. Wang, presented at *2016 38th Annual International Conference of the IEEE Engineering in Medicine and Biology Society (EMBC)*, Florida USA, August **2016**, pp. 6385–6388.